To appear in **Inverse Problems** (2018) https://doi.org/10.1088/1361-6420/aae1e9

Special issue on `*Inverse wave propagation problems without phase information*'

Rough surface reconstruction from phaseless single frequency data at grazing angles

Yuxuan Chen*, Orsola Rath Spivack† and Mark Spivack†

September 17, 2018

Email: yc397@cam.ac.uk, or100@cam.ac.uk, and ms100@cam.ac.uk

Abstract

We develop a method for the reconstruction of a perfectly reflecting rough surface from phaseless measurements of a field arising from single frequency scattering at grazing angles. Formulations are given for both Dirichlet and Neumann boundary conditions, and numerical experiments are presented in which close agreement is found with the exact solution. The approach is a marching method based on the parabolic integral equation, which recovers the surface progressively in range, and is iterated a small number of times to produce the final result. It is found that the approach is robust with respect to spatially localized perturbations and to measurement noise.

1 Introduction

The recovery of surface profiles and environmental parameters is a central challenge in a diverse range of applications [1–3]. These often occur in electromagnetic or acoustic wave scattering [4–8] and it is natural to make use of knowledge of the scattered fields in the inverse problem. Such treatments have introduced a variety of approaches including the Kirchhoff and small height FFT approximations [9, 10], iterative solutions such as [11], integral equation methods [12–15], minimal target technique [16], time domain point source [17], multiple angles [18], and interferometry [19]. Doppler or backscattered multiple frequency radar measurements have also been used in sea state and surface profile retrieval [20–23].

The idealised situation of noiseless and full phase-and-amplitude measurements is not always attainable, and there is a significant need for robust methods in which missing phase information can either be recovered or circumvented [24]. This was tackled in [25], where multiscale surfaces were successfully recovered from phaseless multi-frequency data. The surfaces studied consisted of superposition of typically 5 or 6 sinusoidal spatial components, and Landweber iteration was employed. In another study [26] a recursive Newton iteration was used to recover two-scale and

*Department of Engineering, University of Cambridge, CB2 1PZ, UK
†Centre for Mathematical Sciences, University of Cambridge, CB3 0WA, UK ,

piecewise linear surfaces from intensities of multi-frequency far-field data. A somewhat related problem of two-dimensional target characterization from diffracted intensity was tackled in [27].

In this paper an algorithm is developed for the reconstruction of rough surfaces $h(x)$ from phaseless data arising from a single-frequency incident field. Surfaces may have spatial variation on many roughness scales, and assumptions on surface spectra are not imposed *a priori*. The method is derived for both Dirichlet and Neumann boundary conditions, and exploits the properties of grazing angle scatter. The approach is a marching method, which at the first stage reconstructs the surface progressively in the propagation direction, and then improves the estimate by iterating a small number of times. An analogous approach was previously described in [28] for Dirichlet boundaries but in that case full complex scattered data was required.

For general incident angles the scattered field obeys the Helmholtz boundary integral equation [4, 6, 29]. However, at low grazing angles most energy is forward-scattered and wave propagation is well described by the parabolic equation [30]. Applying this to the governing Green's function allows the Helmholtz integral equations to be replaced by the parabolic integral equation method [31, 32]. Here we use both the Dirichlet [31, 32] and the Neumann forms of the parabolic equation Green's function from Uscinski [33, 34].

To derive the inversion algorithm the problem is in effect formulated as an integral equation in the unknown surface field Φ (which may be the total field or its vertical derivative) treated as a function of the surface. This surface field is in turn related to the amplitude of the scattered data along a line parallel to the mean surface plane, via the introduction of a transformed variable $\theta(h(x))$. Using an expression relating h to Φ, this coupled system is solved directly by numerical inversion. These equations are valid for moderate surface heights and the Volterra form of the integral equation allows us to find the surface progressively along the propagation direction. The incident wave is assumed known, together with scattered data along a line parallel to the mean surface level.

The algorithm is applied here to several types of roughness spectra including rough surfaces consisting of many scales as well as smoother examples with a small number of widely-spaced sinusoidal components. Scattered data is obtained from solution of the full Helmholtz integral equations. It is found that results are robust with respect to noise, and exhibit a type of self-regularization; the resulting perturbations to the reconstructed surfaces are largely delta-correlated and can be effectively filtered out, and noise in one part of the reconstruction does not significantly contaminate results further along the surface as the marching algorithm progresses. Tests of convergence are carried out with respect to initial guess, for different surfaces, boundary conditions and surface autocorrelation lengths, and for multiple realisations.

In Section 2 the parabolic integral equation method is briefly reviewed. The recovery of the surface field data Φ is described in Section 3 and the inversion algorithm is given in Section 4. In Section 5 we apply to algorithm to a number of test cases, and examine there both the error and the effect of adding white noise to the measurement data.

2 Mathematical formulation

Coordinate axes x and z are taken as in Fig. 1 where x is the horizontal and z is the vertical. We

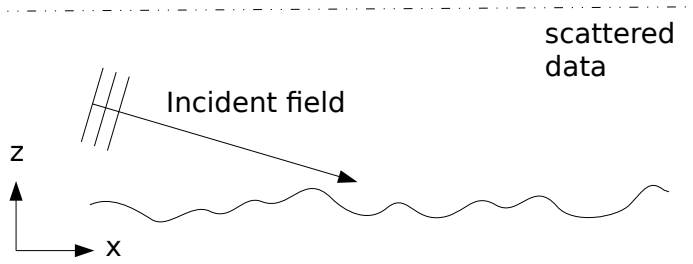

Figure 1: Schematic view of scattering configuration

consider scattering of a time-harmonic wavefield incident from the left on an extended perfectly reflecting rough surface $h(x)$ with mean plane lying along $x = 0$. We will assume the field is incident at low grazing angles resulting in small angles of scatter. The total field E obeys the Helmholtz equation

$$\nabla^2 E(x,z) + k^2 E(x,z) = 0 \tag{1}$$

where k is the wavenumber. The 2-dimensional free space Green's function G_0 is the zero order Hankel function of the first kind, $G_0(\mathbf{r},\mathbf{r}') = (1/4i)H_0^{(1)}(k|\mathbf{r}-\mathbf{r}'|)$.

In what follows we will restrict attention to the region $0 \le x \le L$ for some L; the surface in $x \ge L$ may be rough or flat but is assumed to be without edges or other strong sources of backscatter. Since forward scattering dominates there exists a slowly varying part ψ defined by $\psi(x,z) = E(x,z)\exp(-ikx)$ which satisfies the parabolic wave approximation [30]

$$\frac{\partial \psi}{\partial x} - \frac{i}{2k}\frac{\partial^2 \psi}{\partial z^2} = 0. \tag{2}$$

Denote the incident and scattered wave as ψ_i and ψ_s, so that $\psi = \psi_i + \psi_s$ is the total wave. Under the small-angle, forward-scattering assumption the parabolic equation free space Green's function $G(\mathbf{r},\mathbf{r}')$ can be derived directly from (2) or by approximation of G_0 [31] (see also [33, 35]), given by

$$G(x,z;x',z') = \frac{\alpha}{\sqrt{x-x'}}\exp\left[\frac{ik(z-z')^2}{2(x-x')}\right] \tag{3}$$

when $x' < x$ and $G = 0$ otherwise, where $\alpha = 1/2(i/2\pi k)^{1/2}$.

Coupled integral equations relating the field in the medium to the boundary may be derived for this Green's function by a procedure analogous to that for the Kirchhoff-Helmholtz equations [29, 31], by use of Green's theorem together with the appropriate boundary condition.

If we assume first the Dirichlet boundary condition (corresponding to a transverse electric (TE) field impinging on a perfectly conducting corrugated surface or acoustic scattering from a pressure release surface) the scattered field obeys [31]

$$\psi_i(\mathbf{r}) = -\int_0^x \frac{\partial \psi(\mathbf{r}')}{\partial z} G(\mathbf{r},\mathbf{r}')dx' \tag{4}$$

where $\mathbf{r} = (x, h(x))$ and $\mathbf{r}' = (x', h(x'))$ both lie on the surface, and

$$\psi_s(\mathbf{r}) = \int_0^x \frac{\partial \psi(\mathbf{r}')}{\partial z} G(\mathbf{r},\mathbf{r}')dx' \tag{5}$$

where $\mathbf{r} = (x, z)$ can now be any point in the media.

On the other hand, if we assume the Neumann boundary condition, corresponding to an acoustic hard surface or transverse magnetic (TM) polarized field, the governing equations [33, 34] become

$$\psi_i(\mathbf{r}) = \frac{\phi(\mathbf{r})}{2} + \int_0^x \frac{\partial G(\mathbf{r};\mathbf{r}')}{\partial z'}\phi(\mathbf{r}')dx', \tag{6}$$

where ϕ is the total field on the surface, both $\mathbf{r} = (x, h(x))$, $\mathbf{r}' = (x', h(x'))$ lie on the surface, and

$$\psi_s(\mathbf{r}) = -\int_0^x \frac{\partial G(\mathbf{r};\mathbf{r}')}{\partial z'}\phi(\mathbf{r}')dx', \tag{7}$$

where $\mathbf{r}'$ is again on the surface and $\mathbf{r}$ is now an arbitrary point in the medium. The surface derivative and surface total wave field, $\partial\psi(\mathbf{r}')/\partial z$ and ϕ, are functions of $h(x)$ and we can denote them as $\psi'(x)$ and $\phi(x)$ respectively. Note that the vertical derivative of the Green's function appearing here replaces the normal derivative (which appears in the full Helmholtz equations) under the assumption of the dominance of forward scattering.

The incident wave is taken as a Gaussian beam parallel to the surface

$$\psi_i(x, z) = \frac{w}{(w^2 + 2ix/k)^{1/2}} \exp\left[-\frac{(z - z_0)^2}{w^2 + 2ix/k}\right], \tag{8}$$

where w is the initial width. The source is centred at $(0, z_0)$ with $z_0 > h(x)$, namely the incident wave field amplitude on the surface near $x = 0$ is negligibly small. The illumination pattern along the surface increases from nearly zero to a peak and decays with $1/\sqrt{x}$. The motivation for choosing a Gaussian beam is two-fold: Its closed form lends itself to the analysis here, and it is a physically reasonable model of a source whose direction and width may be adapted.

3 Recovery of surface wavefield

The first step of the reconstruction is to recover the unknown fields at the surface. Depending on the boundary condition this will be either the normal derivative of the total field or the field itself. From this we will subsequently recover the surface itself, as detailed in section 4. The integral domain $[0, L]$ is discretized by N nodes with x_n for $n = 0, 1, \cdots, N$ where $x_0 = 0$ and $x_N = L$. Denote the spacing between each node as $\delta = x_{n+1} - x_n$. The surface field data is calculated via the first integral equations, e.g. (4) and (6). In order to do this, an initial guess $h(x)$ is needed.

3.1 Dirichlet boundary condition

The equation (4) is a Volterra integral equation in $\psi' = \partial\psi(\mathbf{r}')/\partial z$. The discretisation and numerical solution of this equation forms the basis for the inversion algorithm, by allowing $\psi'(x)$ to be expressed explicitly in terms of $h(x)$ at equally-spaced collocation points. This motivates the use of a simple method, which is low-order in spatial step-size but at suitable resolution provides satifactory solution of the direct problem in this regime. Equation (4) is first written as a sum of

n subintegrals for every point $(x_n, h(x_n))$,

$$\psi_i(x_n, h(x_n)) = -\sum_{l=1}^{n} \int_{x_{l-1}}^{x_l} G(x_n, h(x_n); x', h(x'))\psi'(x')dx'.$$

We assume that the surface derivative varies slowly over each subinterval and thus the integral becomes

$$\psi_i(x_n, h(x_n)) = -\sum_{l=1}^{n} \psi'(X_l) \int_{x_{l-1}}^{x_l} G(x_n, h(x_n); x', h(x'))dx'$$

where $X_l = (x_{l-1} + x_l)/2$. *Remark:* Throughout this paper we assume field quantities vary slowly on the scale of the grid. The validity of this assumption derives from the scattering regime: For the unreduced wave E, scales which govern the variation of the field in x are wavelength, surface height and surface correlation length; if significant backscatter is present it introduces interference effects which increase the x-variation, and adequate resolution for the full wave is dictated by the smaller of wavelength and surface length scale. Here though we are concerned with the parabolic equation regime, so backscattering is minimal, the fast-varying component $\exp(ikx)$ has been removed, and slow variation of relevant functions may be ensured by choosing a grid sufficient to resolve the rough surface. The Green's function $G(\mathbf{r}, \mathbf{r}')$ nevertheless requires more careful treatment for small values of $|\mathbf{r} - \mathbf{r}'|$ where it varies rapidly.

For $n = 1, 2, \cdots, N$, this form leads to a linear system

$$A\Phi' = \Phi_i \tag{9}$$

where

$$\begin{aligned} A(n,l) &= -\int_{x_{l-1}}^{x_l} G(x_n, h(x_n); x', h(x'))dx', \quad 1 \le l \le n \le N \\ \Phi' &= [\psi'(X_1), \psi'(X_2), \cdots, \psi'(X_N)] \in \mathbb{C}^N \\ \Phi_i &= [\psi_i(x_1, h(x_1)), \psi_i(x_2, h(x_2)), \cdots, \psi_i(x_N, h(X_N))] \in \mathbb{C}^N \quad . \end{aligned}$$

Note that A is a lower triangular matrix[1] whose inversion is much more efficient than a full matrix. The integral in matrix A is evaluated in two cases. If $l < n$, we further assume that the exponential term can also be treated as constant on each subinterval, and the integral becomes

$$\alpha E(h(x_n); n, l) I_1(n, l)$$

where

$$E(z; n, l) = \exp\left[\frac{ik}{2}\frac{(z - h(X_l))^2}{x_n - X_l}\right]$$

$$\text{and} \quad I_1(n,l) = \int_{x_{l-1}}^{x_l} \frac{1}{\sqrt{x_n - x'}} dx' = 2(\sqrt{x_n - x_l} - \sqrt{x_n - x_{l-1}})$$

If $l = n$, there is a singularity in the integral. First we apply the Taylor expansion on the surface with $h(x') \cong h(x_n) + h'(x_n)(x' - x_n)$, so that the exponent reduces to

$$\frac{ik}{2}\frac{(h(x_n) - h(x'))^2}{x_n - x'} = \frac{ik}{2}h'(x_n)^2(x_n - x').$$

[1]The system (9) is linear in Φ' and Φ_i but of course not in h, upon which A depends

With a change of variable via $\xi = \sqrt{x_n - x'}$ and $dx' = -2\xi d\xi$, the integral takes the form

$$\int_{\sqrt{\delta}}^{0} \alpha \exp\big[\frac{ik}{2}h'(x_n)^2\xi^2\big]\frac{1}{\xi}(-2\xi)d\xi = \int_{0}^{\sqrt{\delta}} 2\alpha \exp\big[\frac{ik}{2}h'(x_n)^2\xi^2\big]d\xi.$$

where again $\delta = x_{n+1} - x_n$ is spatial step size. For computational convenience, we express the above integral in terms of error function. Apply the formula

$$\int e^{ax^2}dx = -\frac{i}{2}\frac{\sqrt{\pi}}{\sqrt{a}}\mathrm{erf}(ix\sqrt{a}), \tag{10}$$

with $a = \frac{ik}{2}h'(x_n)^2$, the integral becomes

$$-\alpha\frac{\sqrt{\pi}}{\sqrt{a}}i\mathrm{erf}(i\sqrt{\delta a}).$$

Therefore, the matrix A can be approximated by

$$A(n,l) = -\begin{cases}\alpha E(h(x_n);n,l)I_1(n,l) & l < n\\ -\alpha\frac{\sqrt{\pi}}{\sqrt{a}}i\mathrm{erf}(i\sqrt{\delta a}) & l = n\end{cases}. \tag{11}$$

3.2 Neumann boundary condition

The approach applied to Neumann boundary condition is similar to Dirichlet case. The small angles of incidence ensures the dominance of the forward propagation. We define $H(\mathbf{r};\mathbf{r}') = \partial G(\mathbf{r};\mathbf{r}')/\partial z'$ with

$$H(\mathbf{r};\mathbf{r}') = \beta\frac{z - z'}{(x - x')^{3/2}}\exp\left[\frac{ik(z - z')^2}{2(x - x')}\right],$$

where $\beta = -i/2\sqrt{ik/2\pi}$. Eq. (6) is still written as a sum of n subintegrals for any node $x_n \in [x_1, x_N]$,

$$\psi_i(x_n, h(x_n)) = \sum_{l=1}^{n}\int_{x_{l-1}}^{x_l}\big(H(x_n;x') + \frac{\delta(x_n - x')}{2}\big)\phi(x')dx'.$$

where δ is the Dirac δ-function. We again assume that the surface field ϕ varies slowly over each subinterval. Thus the surface wavefield ϕ can be treated as constant and then taken out of the subintegrals,

$$\psi_i(x_n, h(x_n)) = \sum_{l=1}^{n}\phi(X_l)\int_{x_{l-1}}^{x_l}\big(H(x_n;x') + \frac{\delta(x_n - x')}{2}\big)dx'.$$

N linear equations are again obtained for $n = 1, 2, \cdots, N$, which results in a $N \times N$ linear system. Denote a vector of size N including the surface wavefield on each node with

$$\Phi = [\phi(X_1), \phi(X_2), \cdots, \phi(X_N)] \in \mathbb{C}^N$$

Hence the linear system is given by

$$B\Phi = \Phi_i \tag{12}$$

where

$$B(n,r) = \begin{cases} \int_{x_{l-1}}^{x_l} H(x_n;x')dx' & l < n \\ \int_{x_{n-1}}^{x_n} H(x_n,h(x_n);x',h(x'))dx' + \frac{1}{2}, & l = n \end{cases} . \tag{13}$$

The matrix B is also lower triangular, which can be inverted efficiently. For $l < n$, under the same assumption that the exponential term varies slowly and can be treated as constant, the integral becomes

$$\beta E(h(x_n);n,l)\int_{x_{l-1}}^{x_l} \frac{h(x_n)-h(x')}{(x_n-x')^{3/2}}dx'.$$

Apply the Taylor expansion on h with $h(x') = h(x_{l-1}) + h'(x_{l-1})(x'-x_{l-1})$, then the remaining integral has the form

$$\begin{aligned} &\int_{x_{l-1}}^{x_l} \frac{h(x_n)-h(x')}{(x_n-x')^{3/2}}dx' = \int_{x_{l-1}}^{x_l} \frac{h(x_n)-h(x_{l-1})-h'(x_{l-1})(x'-x_{l-1})}{(x_n-x')^{3/2}} \\ &= [h(x_n)-h(x_{l-1})]\int_{x_{l-1}}^{x_l} \frac{dx'}{(x_n-x')^{3/2}} - h'(x_{l-1})\int_{x_{l-1}}^{x_l} \frac{x'-x_n+x_n-x_{l-1}}{(x_n-x')^{3/2}}dx' \\ &= L(h(x_n);n,l)I_2(n,l) + h'(x_{l-1})I_1(n,l), \end{aligned} \tag{14}$$

where

$$\begin{aligned} L(z;n,l) &= z - h(x_{l-1}) - h'(x_{l-1})(x_n - x_{l-1}) \\ I_2(n,l) &= \int_{x_{l-1}}^{x_l} \frac{dx'}{(x_n-x')^{3/2}} = \frac{2}{\sqrt{x_n-x_l}} - \frac{2}{\sqrt{x_n-x_{l-1}}} \end{aligned}$$

For $l = n$, to deal with the singularity, the Taylor expansion of $h(x') = h(x_n) + h'(x_n)(x'-x_n)$ is still employed to transform the integral to

$$\int_{x_{l-1}}^{x_l} \beta\frac{h'(x_n)}{(x_n-x')^{1/2}} \exp\big[\frac{ik}{2}h'(x_n)^2(x_n-x')\big]dx' \tag{15}$$

Change of variable via $\xi = (x_n-x')^{1/2}$, eq. (15) turns to

$$\begin{aligned} &\int_{\sqrt{\delta}}^{0} \beta\frac{h'(x_n)^2}{\xi} \exp\big[\frac{ik}{2}h'(x_n)^2\xi^2\big](-2\xi)d\xi \\ &= \int_0^{\sqrt{\delta}} 2\beta h'(x_n)\exp\big[\frac{ik}{2}h'(x_n)^2\xi^2\big]d\xi. \end{aligned}$$

Apply the formula (10), again with $a = \frac{ik}{2}h'(x_n)^2$, then the integral becomes

$$-\beta h'(x_n)\frac{\sqrt{\pi}}{\sqrt{a}} i\mathrm{erf}(\sqrt{a}\sqrt{\delta}i).$$

Finally, the matrix B is given by

$$B(n,l) = \begin{cases} \beta E(h(x_n);n,l)\big[L(h(x_n);n,l)I_2(n,l) + h'(x_{l-1})I_1(n,l)\big], & l < n \\ -\beta h'(x_n)\frac{\sqrt{\pi}}{\sqrt{a}} i\mathrm{erf}(\sqrt{a}\sqrt{\delta}i) + \frac{1}{2}, & l = n \end{cases} . \tag{16}$$

4 Surface reconstruction

After the surface wavefield data has been obtained, the surface reconstruction is carried out by adapting the integral equations and making use of the known scattered wave amplitude.

Suppose that the amplitude $|\psi_s(x_n, Z)|$ of the scattered field is known at each node $x_n \in [x_1, x_N]$ along the plane at a fixed height Z. (The assumption that data points are evenly-spaced and aligned parallel to the mean plane is a convenient simplification but is not central to the principles of the method. In practice one would normally measure the total rather than the scattered field amplitudes but this restriction can also be dropped. See comments and (25-28) below.) We assume that $Z > h(x)$ for all x. The reconstruction is based on a marching method in the propagation (positive x) direction. The details for Dirichlet and Neumann conditions are given separately but the key step for both cases is to define a new unknown

$$\theta_n = \frac{k(Z - h(X_n))^2}{\delta}.$$

If θ_n can be obtained for all n, then the surface can be reconstructed easily

$$h(X_n) = Z - \sqrt{\frac{\theta_n \delta}{k}}. \tag{17}$$

4.1 Dirichlet case

We will describe here the Dirichlet boundary condition; Neumann case is given below. For $x_n \in [x_1, x_N]$, the integral equation (5) is again a summation of subintegrals

$$\psi_s(x_n, Z) = \sum_{l=1}^{n} \int_{x_{l-1}}^{x_l} G(x_n, Z; x', h(x'))\psi'(x')dx'.$$

Under the same assumption that ψ' and the exponential terms can be taken outside the subintegral, the equation becomes

$$\psi_s(x_n, Z) = \sum_{l=1}^{n} \alpha\psi'(X_l)E(Z; n, l)I_1(n, l). \tag{18}$$

If we first consider $n = 1$, and make a further approximation that

$$E(Z; 1, 1) \sim 1 + \frac{ik}{2}\frac{(Z - h(X_1))^2}{x_1 - X_1} = 1 + i\theta_1,$$

then eq. (18) becomes

$$\frac{\psi_s(x_1, Z)}{\alpha\psi'(X_1)I_1(1, 1)} = 1 + i\theta_1.$$

This naive approximation is applied only initially and at $x = 0$ in place of an arbitrary guess; subsequent iterations use the most recent iterate. and results beyond the first few nodes are found to be insensitive to this value. This is consistent with the observation in §5 that localised perturbations do not propagate significantly.

Taking the modulus and squaring both sides, we recover the surface at node 1 from

$$\theta_1 = \sqrt{\left(\frac{|\psi_s(x_1, Z)|}{|\alpha\psi'(X_1)I_1(1,1)|}\right)^2 - 1}. \tag{19}$$

Here and below, the data $|\psi_s|$ are fixed, whereas the surface-dependent values ψ' in the denominator of equation (19) and subsequent equations will change with iteration. For $n \geq 2$, eq. (18) can be written as

$$\psi_s(x_n, Z) = S_n + \alpha\psi'(X_n)E(Z; n, n)I_1(n, n), \tag{20}$$

where

$$S_n = \sum_{l=1}^{n-1} \alpha\psi'(X_l)E(Z; n, l)I_1(n, l).$$

Suppose that we have already obtained $h(X_1), h(X_2), \cdots, h(X_{n-1})$, then S_n becomes known. Taking moduli and squaring both sides of (20), and applying the formula $|z_1 + z_2|^2 = |z_1|^2 + |z_2|^2 + 2\Re\{\bar{z_1}z_2\}$, we have

$$|\psi_s(x_n, Z)|^2 = |S_n|^2 + |\alpha\psi'(X_n)I_1(n, n)|^2 + 2\Re\{\bar{S_n}\alpha\psi'(X_n)E(Z; n, n)I_1(n, n)\}.$$

Expand the real part via the formula $\Re\{z_1z_2\} = \Re\{z_1\}\Re\{z_2\} - \Im\{z_1\}\Im\{z_2\}$, we have

$$\begin{aligned}
&2\Re\{\bar{S_n}\alpha\psi'(X_n)E(Z, n, n)I_1(n, n)\} \\
&= 2\Re\{\bar{S_n}\alpha\psi'(X_n)I_1(n, n)\}\Re\{E(Z; n, n)\} - 2\Im\{\bar{S_n}\alpha\psi'(X_n)I_1(n, n)\}\Im\{E(Z; n, n)\}
\end{aligned}$$

We now apply Euler's equation $E(Z; n, n) = \cos\theta_n + i\sin\theta_n$, to obtain the following equation

$$p_n \cos\theta_n + q_n \sin\theta_n = u_n, \tag{21}$$

where

$$\begin{aligned}
p_n &= 2\Re\{\bar{S_n}\alpha\psi'(X_n)I_1(n, n)\} \\
q_n &= -2\Im\{\bar{S_n}\alpha\psi'(X_n)I_1(n, n)\} \\
u_n &= |\psi_s(x_n, Z)|^2 - |S_n|^2 - |\alpha\psi'(X_n)I_1(n, n)|^2
\end{aligned} \tag{22}$$

Rewrite the equation (21) applying trigonometric identities

$$\sin(\theta_n + \gamma) = \frac{u_n}{\sqrt{p_n^2 + q_n^2}}, \tag{23}$$

where the phase $\gamma \in [0, 2\pi)$ can be uniquely determined by

$$\cos\gamma = \frac{q_n}{\sqrt{p_n^2 + q_n^2}}, \quad \sin\gamma = \frac{p_n}{\sqrt{p_n^2 + q_n^2}}$$

The solution to the equation has the form

$$\theta_n = \arcsin\left(\frac{u_n}{\sqrt{p_n^2 + q_n^2}}\right) - \gamma. \tag{24}$$

Provided the data is sufficiently well-resolved, we can use the assumption of continuity to resolve any phase ambiguities arising from this expression.

The use of ψ_s rather than the more physically realistic ψ is in order to simplify the algorithm; it is straightforward to replace ψ_s by ψ throughout the analysis giving comparable results, as follows: If we write ψ_s in terms of ψ then (20) becomes

$$\psi(x_n, Z) - \psi_i(x_n, Z) = S_n + \alpha\psi'(X_n)E(Z; n, n)I_1(n, n) \tag{25}$$

Take ψ_i on the rhs,

$$\psi(x_n, Z) = \psi_i(x_n, Z) + S_n + \alpha\psi'(X_n)E(Z; n, n)I_1(n, n) \tag{26}$$

Take modulus square both sides, we still get

$$p_n \cos\theta_n + q_n \sin\theta_n = u_n \tag{27}$$

where

$$\begin{aligned} p_n &= 2\Re\{\overline{(\psi_i(x_n, Z) + S_n)}\alpha\psi'(X_n)I_1(n, n)\} \\ q_n &= -2\Im\{\overline{(\psi_i(x_n, Z) + S_n)}\alpha\psi'(X_n)I_1(n, n)\} \\ u_n &= |\psi|^2 - |\psi_i + S_n|^2 - |\alpha\psi'(X_n)I_1(n, n)|^2 \end{aligned} \tag{28}$$

4.2 Neumann case

The treatment of the Neumann problem is similar but with some significant differences of detail. We again aim to obtain the equation of θ_n. Eq. (7) is written as a sum of subintegrals,

$$\psi_s(x_n, Z) = -\sum_{l=1}^{n} \int_{x_{l-1}}^{x_l} H(x_n, Z; x', h(x'))\phi(x')dx'.$$

Under the assumption that ϕ and the exponential terms can be treated as constant over each subinterval, we get

$$\psi_s(x_n, Z) = -\sum_{l=1}^{n} \beta\phi(X_l)E(Z; n, l) \int_{x_{l-1}}^{x_l} \frac{z - h(x')}{(x_n - x')^{3/2}}dx'. \tag{29}$$

For $n = 1$, we apply the direct approximation to the integral, and take the modulus, then

$$|\psi_s(x_1, Z)| = |\beta\phi(X_1)\frac{(Z - h(X_1))\delta}{(\frac{\delta}{2})^{3/2}}|.$$

In this case, the initial height can be obtained directly as

$$h(X_1) = Z - \frac{|\psi_s(x_1, Z)|}{|\beta\phi(X_1)|}\frac{\sqrt{\delta}}{2\sqrt{2}}. \tag{30}$$

For $n \geq 2$, suppose that we know the surface height to $h(X_{n-1})$, then we write equation (29) as

$$\psi_s(x_n, Z) = S_n - \beta\phi(X_n)E(Z; n, n)\int_{x_{n-1}}^{x_n} \frac{Z - h(x')}{(x_n - x')^{3/2}}, \tag{31}$$

where

$$S_n = -\sum_{l=1}^{n-1} \beta\phi(X_n)E(Z; n, l)\int_{x_{l-1}}^{x_l} \frac{Z - h(x')}{(x_n - x')^{3/2}}dx'.$$

Since for $l \leq n-1$, $h(X_l)$ is known, we employ the same argument as in (14) to calculate the integral, so that this sum becomes

$$S_n = -\sum_{l=1}^{n-1} \beta\phi(X_l)E(Z; n, l)[L(Z; n, l)I_2(n, l) + h'(x_{l-1})I_1(n, l)].$$

For the integral on the right in equation (29), we again apply direct approximation, to obtain

$$\psi_s(x_n, Z) = S_n - \beta\phi(X_n)E(Z; n, n)\frac{Z - h(X_n)}{\sqrt{\delta/2}}.$$

Again taking moduli and squaring both sides leads to

$$|\psi_s(x_n, Z)|^2 = |S_n|^2 + |\beta\phi(X_n)\frac{Z - h(X_n)}{\sqrt{\delta/2}}|^2 + 2\Re\{-\bar{S_n}\beta\phi(X_n)\frac{Z - h(X_n)}{\sqrt{\delta/2}}E(Z; n, n)\}.$$

We expand the real part and apply Euler's equation, which gives

$$p_n \cos\theta_n + q_n \sin\theta_n = u_n, \tag{32}$$

where

$$\begin{aligned} p_n &= 2\Re\{-\bar{S_n}\beta\phi(X_n)\frac{Z - h(X_n)}{\sqrt{\delta/2}}\} \\ q_n &= -2\Im\{-\bar{S_n}\beta\phi(X_n)\frac{Z - h(X_n)}{\sqrt{\delta/2}}\} \\ u_n &= |\psi_s(x_n, Z)|^2 - |S_n|^2 - \left|\beta\phi(X_n)\frac{Z - h(X_n)}{\sqrt{\delta/2}}\right|^2. \end{aligned} \tag{33}$$

There remains one term $Z - h(X_n)$ containing the unknown surface height. We again employ the initial guess h_0 to compute the term. When we iterate the procedure as described below this will be replaced by the reconstructed value from the previous step. Equation (32) is then equivalent to the equation,

$$\sin(\theta_n + \gamma) = \frac{u_n}{\sqrt{p_n^2 + q_n^2}}. \tag{34}$$

The same approach as for Dirichlet case can now be used to evaluate the inverse sine function. As described later we have found that the results are relatively insensitive the choice of initial guess. When this produces a good approximation for the approximated surface values ψ' and ϕ, this in turn provides a good surface reconstruction. The reconstructed surfaces thus obtained can substituted back into the algorithm successively, to improve the reconstruction via a small number of iterations as described below.

4.3 Successive improvement

Suppose that we have an initial guess h_0, the surface data ψ_1' and ϕ_1 are recovered via using h_0. The first surface reconstruction h_1 can subsequently obtained by ψ_1' or ϕ_1. This surface h_1 can then substituted back into the whole algorithm to generate new surface data ψ_2' and ϕ_2, which leads to the second surface reconstruction h_2. This procedure can then be repeated.

In all cases we examined we found that only a few iterations (typically 3) leads to satisfactory results, and that (with a few exceptions when there are very sharp spurious peaks) further iteration does not appreciably change the shape of the reconstructed surface. Thus it may be considered a multi-step rather than a fully iterative method.

The procedure is summarised in algorithm (1) below.

Remarks: Although numerical evidence suggests that this process is convergent, rigorous justification for this is lacking. Computationally we find that the residual l_2 error decreases with iteration and that the solution remains stable around the exact solution h_{exact}, i.e. h_{exact} is a fixed point. If we denote the n-th iterate $h_n = h + \epsilon_n$, a heuristic argument to show that $||\epsilon_n|| \to 0$ might go as follows:

The stability at h_{exact} is reasonably apparent from (19)-(24) since, if h_{exact} is the initial input, then updated values of ψ' (and consequently of h) would be unchanged to within numerical errors determined by the discrepencies between exact and numerical solutions of the integral equations.

More generally, functions of h_n appearing the denominator are continuous and bounded away from zero in the regions of interest, so we may expect small perturbations to h_n to give rise to bounded perturbations in Ψ' and thus in the solution. This may suggest a tractable route to obtaining quantitative bounds.

Algorithm 1 Reconstruction of the surface height $h(x)$

```
Input: ν: number of iterations, ψ_i(x, z), ψ_s(x_n, Z) for n = 1, 2, ··· , N
Set h_0 as initial guess
for j = 1, ··· , ν do
    Generate ψ' from AΦ' = Φ_i constructed by eq. (11) or φ from BΦ = Φ_i constructed by eq. (16) using the iterative h
    for n = 1, 2, ··· , N do
        if n = 1 then
            Calculate θ_1 by eq. (19) or (30)
        else
            Generate the equation (23) by finding the coefficients in eq. (22) or (33)
            Solve for θ_n via inverse sine function
        end if
        Reconstruct the surface h(X_n) from eq. (17)
    end for
end for
```

5 Numerical results

A range of numerical examples have been tested to validate the performance of the method, and the procedures have been implemented in Python. The scattered data is obtained from direct solution of the Helmholtz integral equations, as described for example in [36, 37]. For this purpose the full 2-dimensional Green's function G_0 was used, which in contrast to the parabolic equation Green's function is symmetric and allows for arbitrary scattering angles. The computational domain was extended to the right to minimise spurious edge effects. For computational convenience scattered data were obtained at equally spaced grid points x_i along a horizontal line.

Three specific examples are shown here; one is a smoothly varying deterministic 2-component surface, and two are randomly rough surfaces with full roughness spectra. In each of these examples, we take the range of x to be $[0, 300]$ for surface and measurement plane and number of nodes as $N = 800$. The wavenumber is set as $k = 1$ although by renormalising length scales this may represent arbitrary wavelengths. The key scattering scales in the direct problem are the surface height σ and autocorrelation length l with respect to wavelength λ (or equivalently l/σ and $k\sigma$). In the inverse problem the incident wavelengths can in principle be tuned to optimize the algorithms. On the other hand, the non-dimensional ratio of rms surface height to correlation length will be determined by the particular physical regime. The typical surface ranges from about $z = -0.10$ to $z = 0.10$, and the height of the measurement plane is chosen in the results here to be $Z = 1.0$. Note that as it propagates outwards from the surface, the amplitude pattern at each height shifts towards the right (larger x) and the information it carries from the surface will move with it. Thus it is expected that as Z increases we need to shift the measurement domain to examine scattered field at larger x values in order to maintain accuracy. If instead we vary the height and/or the width of the source, a similar issue arises, i.e. the optimal region over which information is carried from the surface will vary. The initial guess is chosen as

$$h_0 = \sin(0.05x)/1000.$$

Example 1. We first take an example of smooth 2-scale surface given by

$$h(x) = (\sin(0.2x) + \sin(0.06x))/20. \tag{35}$$

The reconstructed surfaces at the first and the third iteration are shown in Fig. 2 for Dirichlet and Neumann cases.

The reconstructions fit well with the original surface and recaptures most of detailed features. Moreover, the reconstruction improves significantly through iterations as the surface data ψ' and ϕ improve. By the third iterate, the surface is almost indistinguishable from the exact solution.

Note that the surface reconstructions for the Dirichlet case exhibited rapid transient oscillations within the initial (far-left) region, occupying about $3 - 4\%$ of the overall domain. This was found in all numerical experiments in Dirichlet case. For ease of plotting we have simply set the values to zero, but no artificial damping was used in the calculations themselves.

This oscillation is in part due to the low order approximation $e^{i\theta} \cong 1 + i\theta$ and is exacerbated by the nearly zero amplitudes on the measurement plane around $x = 0$, due to the low scattering angles and domain truncation. However, it is notable that this perturbation does not propagate beyond this region; it is found that the reconstruction tends to stabilize automatically as it progresses

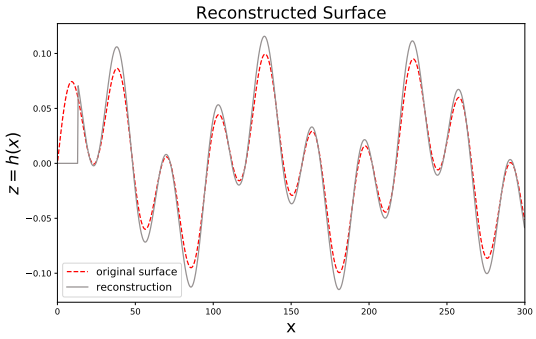

(a) Dirichlet 1^{st} iteration

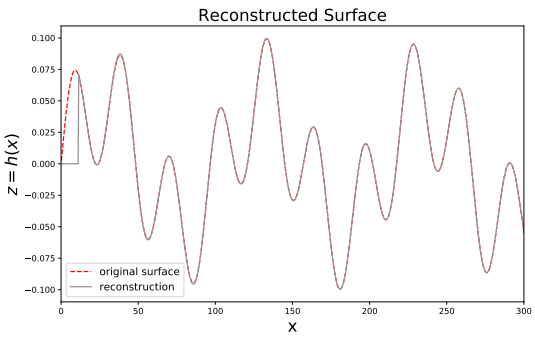

(b) Dirichlet 3^{rd} iteration

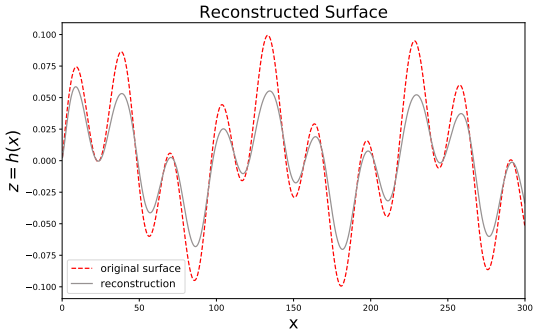

(c) Neumann 1^{st} iteration

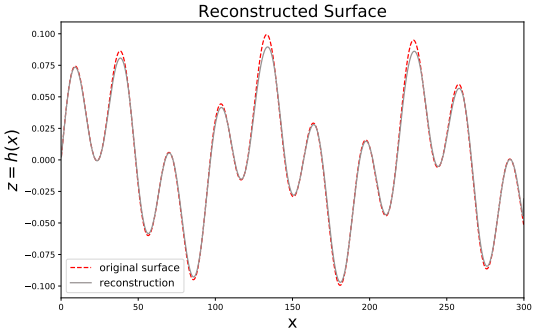

(d) Neumann 3^{rd} iteration

Figure 2: Example 1: plots of reconstructed surfaces for Dirichlet case: (a). at the first iteration, (b). at the third iteration; and Neumann case: (c). at the first iteration, (d). at the third iteration.

in range, in what appears to be a type of self-regularization. This is also found to be the case when noise pollutes the measurements. We remark that a tapered incident field may be used (as for example in [25]) to minimize leading-edge effects, but in our case if the source is located reasonably far above the surface this is unnecessary.

The type of perturbation observed above does not feature in the Neumann case, although overall the reconstruction for Dirichlet is better than the Neumann case since, for a given surface height, a Neumann boundary condition produces stronger scattering. The disparity is related to the nature of the singularity in the Neumann parabolic integral equations, which causes local surface values to dominate and diminishes edge effects from domain truncation [36].

The next two examples are two types of random statistically stationary rough surface. The random rough surface is generated by a given autocorrelation function (a.c.f.) $\rho(\eta)$ for

$$\rho(\eta) = \langle h(x)h(x+\eta)\rangle,$$

where $\eta = x' - x$. In practice, the surface is synthesized by the summation of Fourier modes, with independent random phases chosen uniformly in $[0, 2\pi)$ and a filter function depending on ρ.

Example 2. We take a Gaussian type surface here with the Gaussian a.c.f. given by

$$\rho(\eta) = \sigma^2(-\frac{\eta^2}{l^2}), \tag{36}$$

where $l = 8$ is the surface correlation scale and $\rho(0) = \sigma^2 = 0.1$ is the variance. The reconstructions at the first and the third iteration are shown in Fig. 3 for Dirichlet and Neumann case.

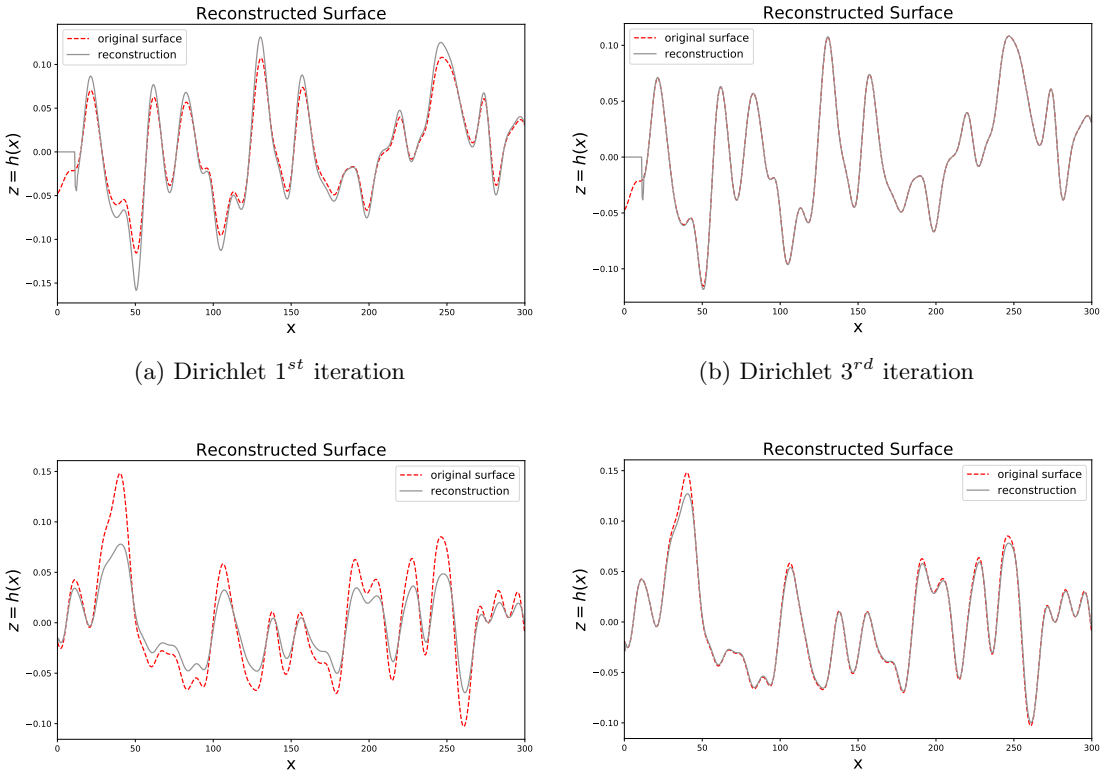

(a) Dirichlet 1^{st} iteration

(b) Dirichlet 3^{rd} iteration

(c) Neumann 1^{st} iteration

(d) Neumann 3^{rd} iteration

Figure 3: Example 2: plots of reconstructed surfaces for Dirichlet case: (a). at the first iteration, (b). at the third iteration; and Neumann case: (c). at the first iteration, (d). at the third iteration.

Similar results are obtained as for Example 1, and the algorithm improves via iterations. The highly oscillatory parts at the initial domain still occur in the experiments of the Dirichlet case. Close agreement with the exact solution is found for both boundary conditions, although results are marginally betters in the Dirichlet case. It is observed that even after 3 iterations in the Neumann case, discrepancies in the reconstructed surface are visible in the vicinity of peaks although overall the results remain very satifactory.

We also test the sensitivity of the algorithm to the addition of white noise to the scattered data. More specifically, independent Gaussian-distributed random noise of complex values $\epsilon_r + i\epsilon_r$ were added to the full complex scattered data, before taking the amplitude. This noise was was

added throughout the spatial domain, including initial regions where the original data was near zero, where it might be expected to have a greatly disproportionate effect. The measurement noise results in significant noisy perturbations across the whole domain. However, these components are qualitatively similar to the white noise itself. In order to remove these oscillations, we applied a simple filtering procedure by a five-point moving average. This is adequate provided the surface is smooth enough on the smallest scale size of the grid. Comparison between actual and filtered reconstructed surfaces for 1% and 3% noise added to Dirichlet and Neumann scattered data are shown in Fig. 4.

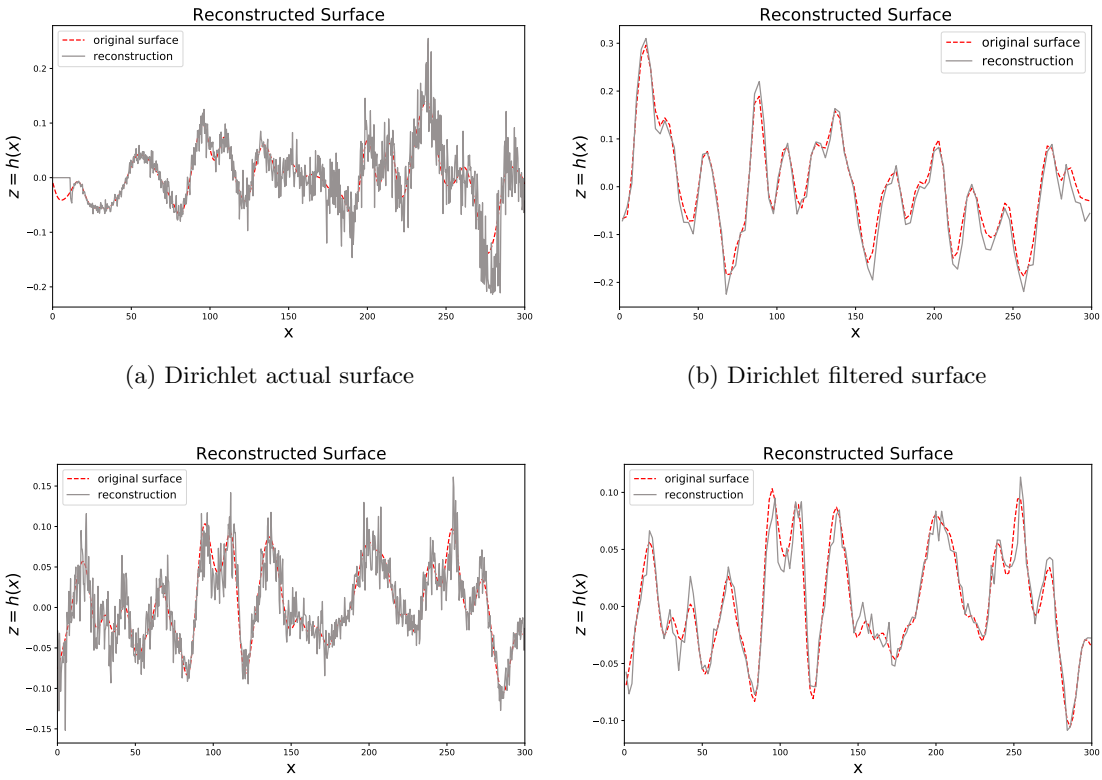

(a) Dirichlet actual surface

(b) Dirichlet filtered surface

(c) Neumann actual surface

(d) Neumann filtered surface

Figure 4: Example 2: plots of the reconstructed surface at the third iteration for noise level of 1% added to the Dirichlet scattered data: (a) actual surface, (c) filtered surface; and for noise level of 3% added to the Neumann scattered data: (a) actual surface, (c) filtered surface.

Before any filtering, the main surface variation is very clear although it is apparent particularly in the region of surface peaks the noise-induced perturbation is also highly peaked. After filtering, although the surface reconstruction retains some small scale inaccuracies, it is still able to capture the features of the original surface in considerable detail.

Example 3. We take a sub-fractal type random surface with an a.c.f. given by

$$\rho(\eta) = \sigma^2(1 + \frac{|\eta|}{l}) \exp(-\frac{|\eta|}{l}). \tag{37}$$

This is a relatively jagged surface with peaks on a small horizontal scale. The reconstructions at the first and the third iteration are shown in Fig.5.

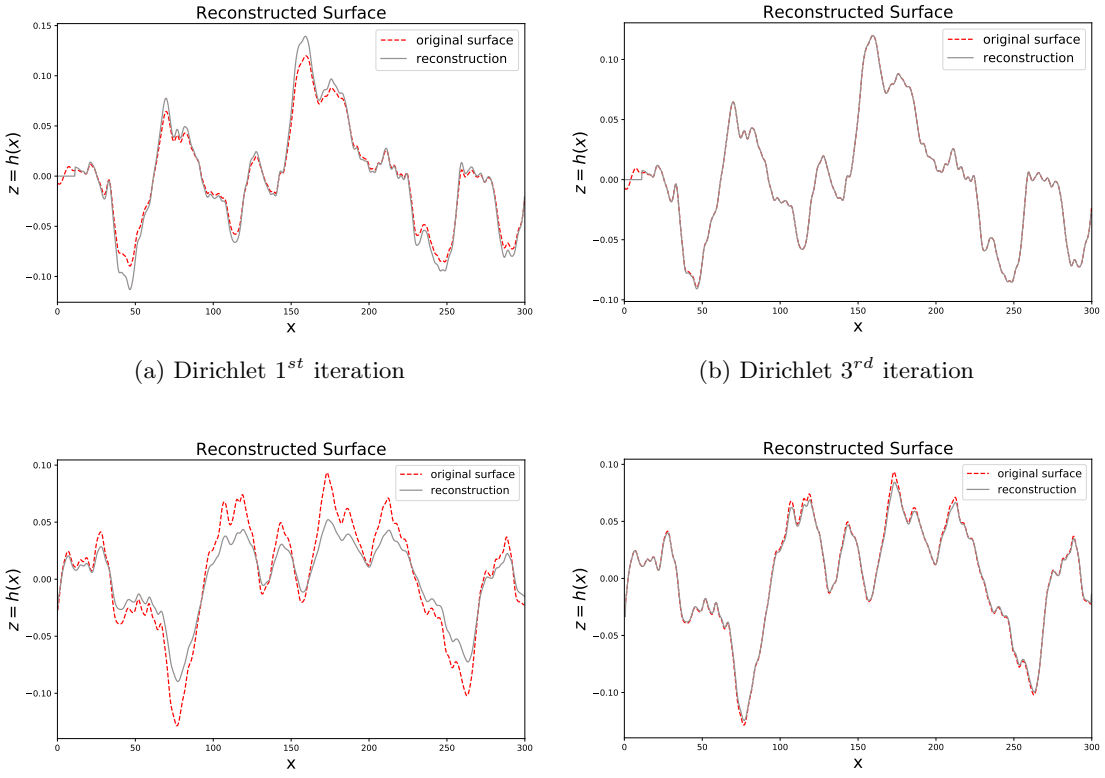

(a) Dirichlet 1^{st} iteration

(b) Dirichlet 3^{rd} iteration

(c) Neumann 1^{st} iteration

(d) Neumann 3^{rd} iteration

Figure 5: Example 3: plots of reconstructed surfaces for Dirichlet case: (a). at the first iteration, (b). at the third iteration; and Neumann case: (c). at the first iteration, (d). at the third iteration.

The results are again similar to the previous examples. Except for the initial oscillatory regions, the reconstruction for Dirichlet case works somewhat better than for the Neumann case. On the other hand, the sub-fractal surface is much more complicated due to the rapid variation at small scales. The method shows its ability to recapture all of these small peaks well especially at the third iteration. The same noise test is used here. We again apply 1% noise to the Dirichlet scattered and 3% noise to the Neumann scattered data. Comparison between actual and filtered surfaces are shown in Fig. 6.

The surface reconstruction is obtained as before with a rapdily varying perturbation, although the main surface details are again clear. As might be expected smaller-scale surface features

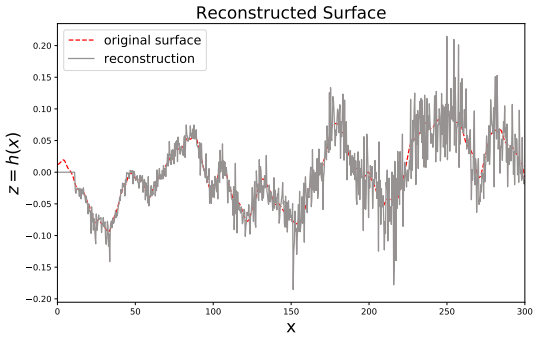

(a) Dirichlet actual surface

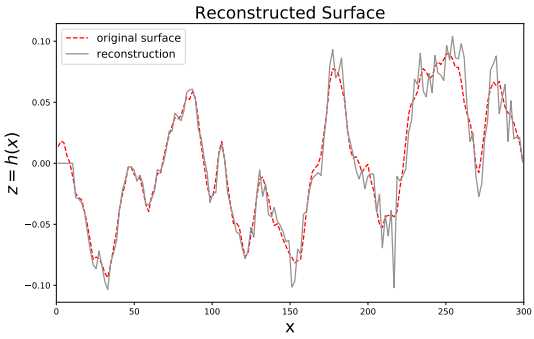

(b) Dirichlet filtered surface

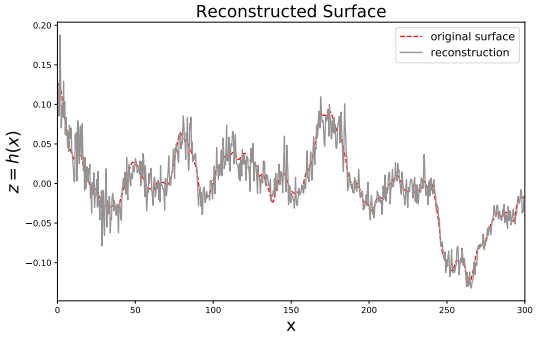

(c) Neumann actual surface

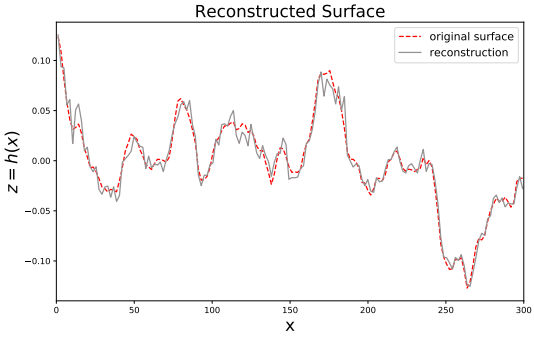

(d) Neumann filtered surface

Figure 6: Example 3: plots of the reconstructed surface at the third iteration for noise level of 1% added to the Dirichlet scattered data: (a) actual surface, (c) filtered surface; and for noise level of 3% added to the Neumann scattered data: (a) actual surface, (c) filtered surface.

are more difficult to resolve fully. After applying the simple filtering, the reconstruction closely recaptures the main features, although it remains slightly oscillatory. Compared to the Gaussian-type surface, the reconstruction for sub-fractal autocorrelation therefore performs marginally less well.

We also present the relative error in l_2 norm for the reconstructions, which is given by

$$e_j = \frac{\|h_j - \bar{h}\|_{l_2}}{\|\bar{h}\|_{l_2}}, \tag{38}$$

where $\bar{h}$ is the exact surface, and j refers to the number of iteration. First, Table 1 gives the error for the examples shown above. Clearly, the error decreases through iterations. The error is larger in Dirichlet case due to the initial oscillatory region (calculated but not shown). We further tested the algorithm with respect to the different initial guesses $h_0(x)$. It is noted that this initial function cannot be a constant due to the surface derivative in the denominator shown in the error function term. We have tested different initial guesses varying the scale sizes of $h_0(x)$, and have

	Dirichlet example			Neumann example		
Iteration	1	2	3	1	2	3
e_1	0.2990	0.3189	0.2565	0.3567	0.3576	0.3411
e_2	0.2629	0.2374	0.1295	0.1409	0.1438	0.1297
e_3	0.2236	0.1945	0.1215	0.0609	0.0643	0.0534

Table 1: Error of reconstructed surfaces in surface examples 1 to 3 (2-scale, Gaussian, sub-fractal) where e_j denotes the error at the j-th iteration

found that the results are relatively insensitive to this. Table 2 shows the error in the various cases, where we have averaged Examples 2 and 3 (Gaussian and sub-fractal random surfaces) over several realisations. The following initial functions are employed,

$$h_0^a = \sin(0.05x)/1000$$
$$h_0^b = \sin(0.05x)/10$$
$$h_0^c = \sin(0.1x)/1000$$
$$h_0^d = \sin(0.1x)/10$$

2-scale	Dirichlet				Neumann			
Iteration	a	b	c	d	a	b	c	d
e_1	0.299	0.474	0.299	0.590	0.357	0.562	0.357	0.617
e_2	0.263	0.268	0.263	0.277	0.141	0.195	0.141	0.229
e_3	0.224	0.224	0.224	0.224	0.0609	0.0743	0.0610	0.0921
Gaussian	Dirichlet				Neumann			
Iteration	a	b	c	d	a	b	c	d
$\langle e_1 \rangle$	0.272	0.347	0.250	0.358	0.378	0.633	0.363	0.586
$\langle e_2 \rangle$	0.226	0.204	0.188	0.211	0.162	0.233	0.144	0.219
$\langle e_3 \rangle$	0.194	0.179	0.162	0.183	0.0779	0.0989	0.0662	0.0911
Sub-fracal	Dirichlet				Neumann			
Iteration	a	b	c	d	a	b	c	d
$\langle e_1 \rangle$	0.272	0.340	0.260	0.372	0.359	0.565	0.339	0.597
$\langle e_2 \rangle$	0.199	0.198	0.191	0.166	0.146	0.188	0.128	0.215
$\langle e_3 \rangle$	0.195	0.196	0.187	0.161	0.0701	0.0713	0.0721	0.0872

Table 2: Error of reconstructed surfaces with respect to the initial guess (a,b,c, or d)

For different initial guesses, the reconstruction at the first iteration is influenced the most. The error obtained at the third iteration is similar. With a smaller scale of initial guess, the method produces a better result at the first iteration. There is no obvious trend of effects of different wavelength of initial guess.

Finally we examined the capability of dealing with different surface correlation scales l. This corresponds to varying the scattering regime, since this is determined by the ratio of horizontal scale to surface height, and surface height to wavelength. As l increases, the surface becomes smoother.

The sub-fractal surfaces (Example 3) are employed, which are also the most complicated. With larger l, those peaks on small scales, on the contrary, become denser. The fig. 7 and 8 show the reconstructions at the third iteration for different l.

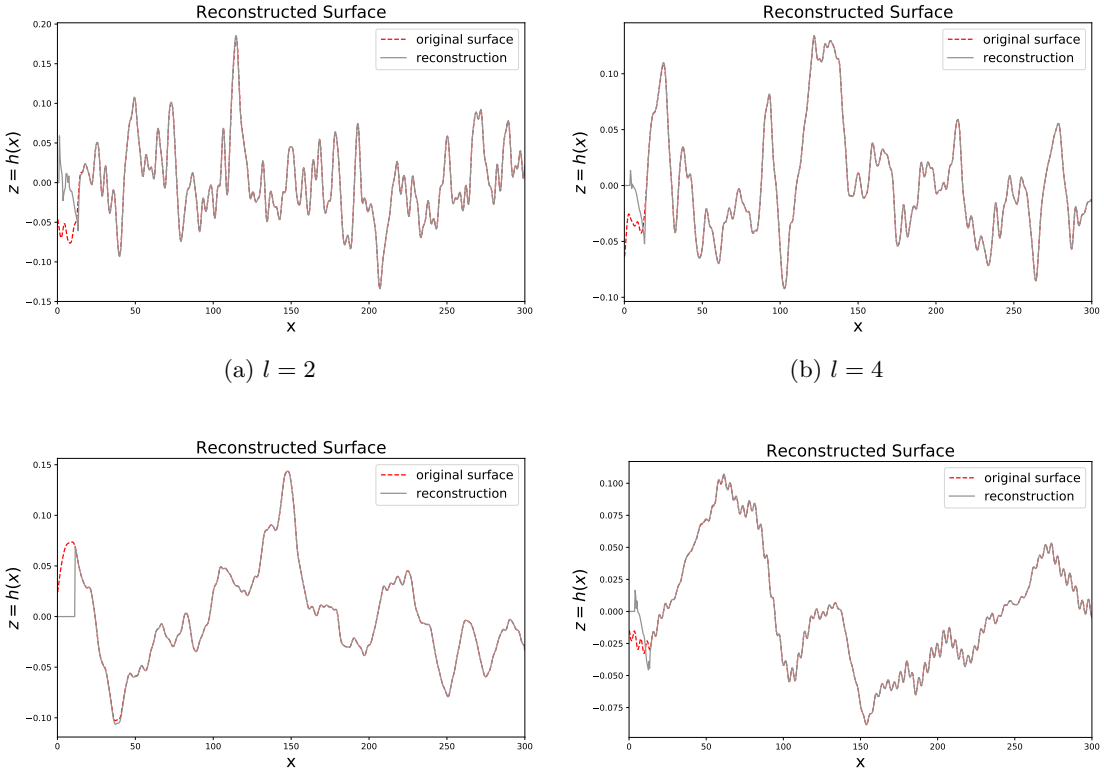

(a) $l = 2$ (b) $l = 4$

(c) $l = 8$ (d) $l = 16$

Figure 7: Example 3 Dirichlet case: plots of reconstructions at the third iteration with different surface correlation scales

It is clear that the method works well for all of these surface correlation lengths, and in each case by the third iteration these reconstructions recapture most features of the original surfaces. The relative error for different correlation scales obtained in both Example 2 and Example 3 is listed in Table 3.

6 Conclusions

We have developed an approach to recover rough surface profiles from single-frequency scattered wave amplitudes, in the absence of phase information. This is applied when the incident wave field is at low grazing angles to the surface so that forward scatter predominates. The approach is an extension of an iterated marching method which was previously available only for full complex am-

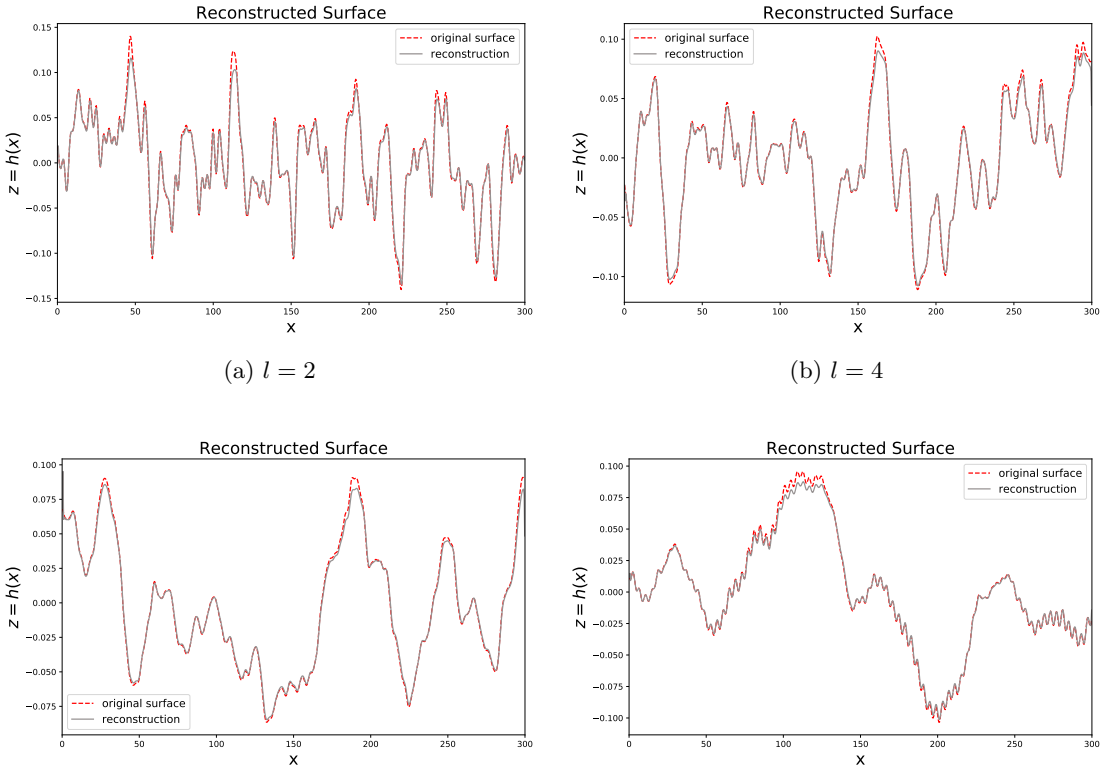

(a) $l = 2$ (b) $l = 4$

(c) $l = 8$ (d) $l = 16$

Figure 8: Example 3 Neumann case: plots of reconstructions at the third iteration for different surface correlation scales

plitude measurements. Versions are derived for both Dirichlet and Neumann boundary conditions. In this method, which makes use of the parabolic wave equation, starting from an initial guess, surface values are obtained progressively along the propagation direction. This is iterated a small number of times (typically three). An important and perhaps surprising finding is that errors at the start of this domain do not significantly propagate to contaminate the later values, so that the method shows a type of self-regularisation.

We have conducted numerical experiments for a number of different surface spectra, and examined the robustness with respect to measurement noise. The examples treated include smoothly varying 2-scale surfaces and randomly rough surfaces with a many components over a range of length scales. In all the cases considered good agreement has been obtained between exact and reconstructed surfaces. Interesting differences emerge between Dirichlet and Neumann conditions. In the Dirichlet case rapid oscillations occur in the initial reconstructions at the start of the range which nevertheless allow accurate results over most of the range. This does not occur with Neumann condition. The addition of random white noise to the measurements leads to noisy reconstructions, in which the main surface features are clearly reproduced but with a rapidly varying perturbation.

surface correlation scale	Ex.2 Dirichlet	Ex.2 Neumann	Ex.3 Dirichlet	Ex.3 Neumann
l=1	0.252	0.166	0.238	0.120
l=2	0.228	0.149	0.233	0.0997
l=4	0.207	0.101	0.204	0.0890
l=8	0.194	0.0779	0.195	0.0701
l=12	0.142	0.0747	0.162	0.0582
l=16	0.0848	0.0475	0.121	0.0478

Table 3: Averaged error at the third iteration for different surface correlation lengthscales

This perturbation has length scales small enough that it can be removed by simple filtering, so that the filtered reconstruction agrees closely with the exact solution.

In order to simplify the algorithm the measurements were assumed to be at evenly spaced points aligned parallel to the mean plane, but this is not needed for the basic principles of the method. We do not yet have rigorous results for the convergence of iterates under this method; such results are an aim of future work. Reconstruction of finite impedance or penetrable surfaces appears to be beyond the scope of this approach, although work is in progress on the full 3-dimensional problem in the perfectly reflecting case.

Ackowledgments

The authors are grateful to the referees for numerous helpful comments and suggestions.

References

[1] Peter de Groot. Principles of interference microscopy for the measurement of surface topography. *Advances in Optics and Photonics*, 7(1):1–65, 2015.

[2] Parameswaran Hariharan. *Optical interferometry*. Academic press, 2003.

[3] Susumu Kuwamura and Ichirou Yamaguchi. Wavelength scanning profilometry for real-time surface shape measurement. *Applied optics*, 36(19):4473–4482, 1997.

[4] Karl F Warnick and Weng Cho Chew. Numerical simulation methods for rough surface scattering. *Waves in Random Media*, 11(1):R1–R30, 2001.

[5] AG Voronovich. *Wave scattering from rough surfaces*, volume 17. Springer Science & Business Media, 2013.

[6] M Saillard and A Sentenac. Rigorous solutions for electromagnetic scattering from rough surfaces. *Waves in Random Media*, 11(3):103–137, 2001.

[7] JM Elson, JP Rahn, and JM Bennett. Relationship of the total integrated scattering from multilayer-coated optics to angle of incidence, polarization, correlation length, and roughness cross-correlation properties. *Applied Optics*, 22(20):3207–3219, 1983.

[8] DL Jordan and F Moreno. Enhanced backscattering and cross depolarization from multiscale surfaces. *JOSA A*, 10(9):1989–1995, 1993.

[9] RJ Wombell and John A DeSanto. The reconstruction of shallow rough-surface profiles from scattered field data. *Inverse Problems*, 7(1):L7, 1991.

[10] Richard J Wombell and John A DeSanto. Reconstruction of rough-surface profiles with the kirchhoff approximation. *JOSA A*, 8(12):1892–1897, 1991.

[11] Ibrahim Akduman, Rainer Kress, and Ali Yapar. Iterative reconstruction of dielectric rough surface profiles at fixed frequency. *Inverse Problems*, 22(3):939, 2006.

[12] Ya-Qiu Jin and Zhongxin Li. Reconstruction of roughness profile of fractal surface from scattering measurement at grazing incidence. *Journal of Applied Physics*, 89(3):1922–1926, 2001.

[13] Ya-Qiu Jin. Reconstruction of a heterogeneous fractal surface profile from scattering measurements at low grazing incidence. In *Antennas and Propagation Society International Symposium, 2005 IEEE*, volume 3, pages 445–448. IEEE, 2005.

[14] M Spivack. Solution of the inverse-scattering problem for grazing incidence upon a rough surface. *J. Opt. Soc. Am. A*, 9(8):1352–1355, 1992.

[15] M Spivack. Direct solution of the inverse problem for rough surface scattering at grazing incidence. *Journal of Physics A: Mathematical and General*, 25(11):3295, 1992.

[16] Zhijie Cai, Deqiang Chen, and Shuai Lu. Reconstruction of a fractal rough surface. *Physica D: Nonlinear Phenomena*, 213(1):25–30, 2006.

[17] Claire D Lines and Simon N Chandler-Wilde. A time domain point source method for inverse scattering by rough surfaces. *Computing*, 75(2-3):157–180, 2005.

[18] Mehmet Cayoren, Ibrahim Akduman, Ali Yapar, and Lorenzo Crocco. Shape reconstruction of perfectly conducting targets from single-frequency multiview data. *IEEE Geoscience and Remote Sensing Letters*, 5(3):383–386, 2008.

[19] Peter de Groot and Leslie Deck. Surface profiling by analysis of white-light interferograms in the spatial frequency domain. *Journal of modern optics*, 42(2):389–401, 1995.

[20] Joel T Johnson, Robert J Burkholder, Jakov V Toporkov, David R Lyzenga, and William J Plant. A numerical study of the retrieval of sea surface height profiles from low grazing angle radar data. *IEEE Transactions on Geoscience and Remote Sensing*, 47(6):1641–1650, 2009.

[21] Okey G Nwogu and David R Lyzenga. Surface-wavefield estimation from coherent marine radars. *IEEE Geoscience and Remote Sensing Letters*, 7(4):631–635, 2010.

[22] David R Lyzenga, Okey G Nwogu, Robert F Beck, Andrew O'Brien, Joel Johnson, Tony de Paolo, and Eric Terrill. Real-time estimation of ocean wave fields from marine radar data. In *Geoscience and Remote Sensing Symposium (IGARSS), 2015 IEEE International*, pages 3622–3625. IEEE, 2015.

[23] Domenico Schiavulli, Ferdinando Nunziata, Giovanni Pugliano, and Maurizio Migliaccio. Reconstruction of the normalized radar cross section field from gnss-r delay-doppler map. *IEEE Journal of Selected Topics in Applied Earth Observations and Remote Sensing*, 7(5):1573–1583, 2014.

[24] Michele D'Urso, Kamal Belkebir, Lorenzo Crocco, Tommaso Isernia, and Amélie Litman. Phaseless imaging with experimental data: facts and challenges. *JOSA A*, 25(1):271–281, 2008.

[25] Gang Bao and Lei Zhang. Shape reconstruction of the multi-scale rough surface from multi-frequency phaseless data. *Inverse Problems*, 32(8):085002, 2016.

[26] Bo Zhang and Haiwen Zhang. Imaging of locally rough surfaces from intensity-only far-field or near-field data. *Inverse Problems*, 33(5):055001, 2017.

[27] Amélie Litman and Kamal Belkebir. Two-dimensional inverse profiling problem using phaseless data. *JOSA A*, 23(11):2737–2746, 2006.

[28] Yuxuan Chen and Mark Spivack. Rough surface reconstruction at grazing angles by an iterated marching method. *JOSA A*, 35(4):504–513, 2018.

[29] JA DeSanto. Exact boundary integral equations for scattering of scalar waves from infinite rough interfaces. *Wave Motion*, 47(3):139–145, 2010.

[30] F D Tappert. The parabolic approximation method. In *Wave propagation and underwater acoustics*, pages 224–287. Springer, 1977.

[31] E I Thorsos. Rough surface scattering using the parabolic wave equation. *J. Acoust. Soc. Am.*, 82(S1):S103–S103, 1987.

[32] M Spivack. A numerical approach to rough-surface scattering by the parabolic equation method. *J. Acoust. Soc. Am.*, 87(5):1999–2004, 1990.

[33] BJ Uscinski. Sound propagation with a linear sound-speed profile over a rough surface. *The Journal of the Acoustical Society of America*, 94(1):491–498, 1993.

[34] M Spivack and BJ Uscinski. Numerical solution of scattering from a hard surface in a medium with a linear profile. *The Journal of the Acoustical Society of America*, 93(1):249–254, 1993.

[35] RSMS Awadallah. *Rough surface scattering and propagation over rough terrain in ducting environments*. PhD thesis, Virginia Tech, 1998.

[36] M Spivack, A Keen, J Ogilvy, and C Sillence. Validation of left–right method for scattering by a rough surface. *Journal of Modern Optics*, 48(6):1021–1033, 2001.

[37] M Spivack and O Rath Spivack. Rough surface scattering via two-way parabolic integral equation. *Progress in Electromagnetics Research M*, 56:81–90, 2017.